Assessing and Simulating Impacts of Land Use Land Cover Changes on Land Surface Temperature in Mymensingh City, Bangladesh

Tahmid Anam Chowdhury[1] and Md. Saiful Islam[2*]

[1]Department of Geography and Environment, Shahjalal University of Science and Technology, Sylhet-3114, Bangladesh
[2]EQMS Consulting Limited, House 53, Road 04, Block-C, Banani, Dhaka-1213, Bangladesh

ARTICLE INFO

Received: 18 Jun 2021
Received in revised: 30 Oct 2021
Accepted: 15 Nov 2021
Published online: 26 Nov 2021
DOI: 10.32526/ennrj/20/202100110

Keywords:
Land Use Land Cover/ Land surface temperature/ Urban growth/ Simulating LST/ Simulating LULC/ Mymensingh

*** Corresponding author:**
E-mail: mdsaiful91@gmail.com

ABSTRACT

Urban developments in the cities of Bangladesh are causing the depletion of natural land covers over the past several decades. One of the significant implications of the developments is a change in Land Surface Temperature (LST). Through LST distribution in different Land Use Land Cover (LULC) and a statistical association among LST and biophysical indices, i.e., Urban Index (UI), Bare Soil Index (BI), Normalized Difference Builtup Index (NDBI), Normalized Difference Bareness Index (NDBaI), Normalized Difference Vegetation Index (NDVI), and Modified Normalized Difference Water Index (MNDWI), this paper studied the implications of LULC change on the LST in Mymensingh city. Landsat TM and OLI/TIRS satellite images were used to study LULC through the maximum likelihood classification method and LSTs for 1989, 2004, and 2019. The accuracy of LULC classifications was 84.50, 89.50, and 91.00 for three sampling years, respectively. From 1989 to 2019, the area and average LST of the built-up category has been increased by 24.99% and 7.6ºC, respectively. Compared to vegetation and water bodies, built-up and barren soil regions have a greater LST each year. A different machine learning method was applied to simulate LULC and LST in 2034. A remarkable change in both LULC and LST was found through this simulation. If the current changing rate of LULC continues, the built-up area will be 59.42% of the total area, and LST will be 30.05ºC on average in 2034. The LST in 2034 will be more than 29ºC and 31ºC in 59.64% and 23.55% areas of the city, respectively.

1. INTRODUCTION

The extent of urbanization is growing very fast around the world, along with associated infrastructure. By 2030, it is estimated that around 60% of the world's population will be living in cities (UNHABITAT, 2016). Since population growth is a primary driving factor of urbanization, Bangladesh has a rapid increase of urbanization in line with thriving global trends (BBS, 2011). In 2017, about 4.1 billion (with 3.23% annual growth) people lived in the urban areas where it was only 1.02 billion in 1960 (UN, 2017). The world's population is predicted to grow by 2 billion in the next 30 years, from 7.7 billion today to 9.7 billion in 2050, resulting in an increased need for urban infrastructure (UN, 2019). Both vertical and horizontal expansion is happening in cities to fulfill this demand that finally causes changes to the natural landscape and environment by replacing vegetation, wetlands, and arable lands with an urban impervious surface (Bahi et al., 2016; UNHABITAT, 2016). This form of Land Use Land Cover (LULC) shift has negative consequences for the land, the ecosystem, and the urban microclimate (World Bank, 2018; McCarthy et al., 2010). The Land Surface Temperature (LST) and the formation of Urban Heat Island (UHI) are influenced by the LULC variation over time (Kikon et al., 2016; Maimaitiyiming et al., 2014). An urban heat island is where the temperature is greater than it is in the surrounding areas. It is an environmental phenomenon, which is deeply related to the LST (Trenberth, 2004; Voogt and Oke, 2003). The LST shows how the earth's surface energy changes throughout time (Kayet et al., 2016). It varies based on

Citation: Chowdhury TA, Islam MS. Assessing and simulating impacts of land use land cover changes on land surface temperature in Mymensingh City, Bangladesh. Environ. Nat. Resour. J. 2022;20(2):110-128. (https://doi.org/10.32526/ennrj/20/202100110)

LULC categories and their thermal characteristics caused by energy radiation and absorption (Ahmed et al., 2013; Kayet et al., 2016). LST, like LULC, is a significant metric for monitoring vegetation, climatic change, and changes in built-up areas. (Kayet et al., 2016). The typical LST in a UHI is equal to or more than 2ºC compared to its adjacent areas or suburbs (Lai and Cheng, 2010). Different factors, such as a linear and perpendicular expansion of concrete surfaces, open space within buildings, building materials, location of public places, highways, central business district, major and minor industrial hubs, and others, have a significant impact on the accumulation of temperature in the urban surface (Ahmed et al., 2013; Pal and Ziaul, 2017).

Many studies have been undertaken on a global scale to analyze the relationship between LULC and LST using GIS and Remote Sensing techniques, with multi-temporal satellite imageries such as Landsat and MODIS being commonly employed as data sources (e.g., Ahmed et al., 2013; Bokaie et al., 2016; Dewan and Corner, 2014a; Gazi et al., 2020; Kafy et al., 2020; Kayet et al., 2016; Maduako et al., 2016; Pal and Ziaul, 2017; Rahman et al., 2017; Rashid et al., 2021; Roy et al., 2020; Ullah et al., 2019; Vani and Prasad, 2020; Zareie et al., 2016; Zhang et al., 2016). Such imageries provide both spectral and thermal bands where the spectral band is used to detect LULC, and the thermal band is used for LST estimation. The estimation of both LULC and LST of the same position simultaneously is very efficient for this kind of analysis. The majority of these researches focused on the effects of LULC changes on LST and the link between biophysical parameters (i.e., NBDI, NDVI, etc.) and LST (e.g., Bokaie et al., 2016; Dewan and Corner, 2014a; Kayet et al., 2016; Pal and Ziaul, 2017; Rashid et al., 2021; Roy et al., 2020; Ullah et al., 2019; Vani and Prasad, 2020; Zareie et al., 2016; Zhang et al., 2016). Also, simulation has been conducted to predict LULC and LST in a few studies (e.g., Ahmed et al., 2013; Kafy et al., 2020; Maduako et al., 2016; Ullah et al., 2019). The excellent accuracy level of the Multi-Layer Perceptron-Markov Chain (MLP-MC) approach for simulating the LULC makes the predictions based on the LULC change trend of previous years more accurate (Ahmed and Ahmed, 2012; Al-sharif and Pradhan, 2014; Corner et al., 2014). Simulating continuous data, such as LST using the ANN method, on the other hand, is effective (Ahmed et al., 2013; Kafy et al., 2020; Maduako et al., 2016; Ullah et al., 2019). Previous studies on LULC and LST in urban areas have found that increasing built-up areas while decreasing natural land covers has resulted in a net rise in LST. A substantial relationship has also been discovered between LST and several indices, such as built-up/urban, vegetation, and water index.

In the context of Bangladesh, some studies have been accomplished on both LULC and LST change covering a few cities like Dhaka, Chattogram, and Rajshahi (e.g., Ahmed et al., 2013; Dewan and Corner, 2014a; Gazi et al., 2020; Kafy et al., 2020; Roy et al., 2020), but simulation has been conducted in Dhaka and Rajshahi only (e.g., Ahmed et al., 2013; Kafy et al., 2020). A study has been undertaken on vegetation and LST change in selected regions of Cox's Bazar District as a result of the Rohingya immigration, in addition to urban areas (Rashid et al., 2021). From the view of the LST derivation method, very few studies have applied a split-window algorithm for Landsat 8 in Bangladesh (Gazi et al., 2020; Roy et al., 2020), and only Gazi et al. (2020) has performed validation of LST data derived from Landsat. The rest of the studies have mainly applied both mono-window and single-channel algorithms for Landsat 5, 7, and 8 (Ahmed et al., 2013; Dewan and Corner, 2014a; Kafy et al., 2020; Rashid et al., 2021).

Mymensingh is an old city, which was recognized as a municipal in 1869. As far as it is known, no study has been conducted on this city integrating both LULC and LST change. Since the urban population of Mymensingh city has become double in 1981, the city has been experiencing significant development and degradation of natural land cover since the 1980s (Rouf and Jahan, 2007). The required Landsat satellite images are available from 1989 to study both LULC and LST of Mymensingh city. Therefore, the present study has examined the LULC and LST change from spatial and temporal dimensions using Landsat satellite images over the past thirty years (from 1989 to 2019). The Split-window algorithm for Landsat 8 was used to compute LST in this work, which has only been used in a few earlier studies in Bangladesh and LST validation. This study aims to predict LULC and LST of the year 2034 through simulation. This aim will be achieved through fulfilling these specific objectives: (i) to examine the spatial-temporal changes in LULC and LST, and (ii) to investigate relationships amongst these two variables.

2. METHODOLOGY

2.1 Study area

Mymensingh city is one of the divisional cities in Bangladesh. Geographically, it is situated on the bank of the old Brahmaputra River in Bangladesh's northern region (24 45'N latitude and 90 23'E longitude) (Alam and Haque, 2018). Akua Union surrounds it in the south, Khagdahar Union in the west, Char Ishwardia Union in the north, and Bhabkhali Union in the east. It has elevations varying from +2 to +39 m.m.s.l. (meter mean sea level). The average land height is +16.08 m.m.s.l. Mymensingh city is under the Brahmaputra-Jamuna Floodplain physiographic region and Non-Calcareous Dark Grey Floodplain soil zone (Brammer, 1996; Brammer, 2012). It has Chandina alluvium surface deposits during Holocene (Alam et al., 1990). The city was founded in 1869, and now it covers a total area of 23.16 km^2 (2,316 ha) with 21 administrative wards (Alam and Haque, 2018). It has a population of 258,040 people (male 132,123 and female 125,917) and is growing at a pace of 1.82 percent per year (BBS, 2011). The average temperature of Mymensingh is 25.62ºC, with total annual rainfall ranging from 1,500 to 3,300 mm (BMD, 2019). Figure 1 depicts a city map showing the boundaries of various administrative subdivisions.

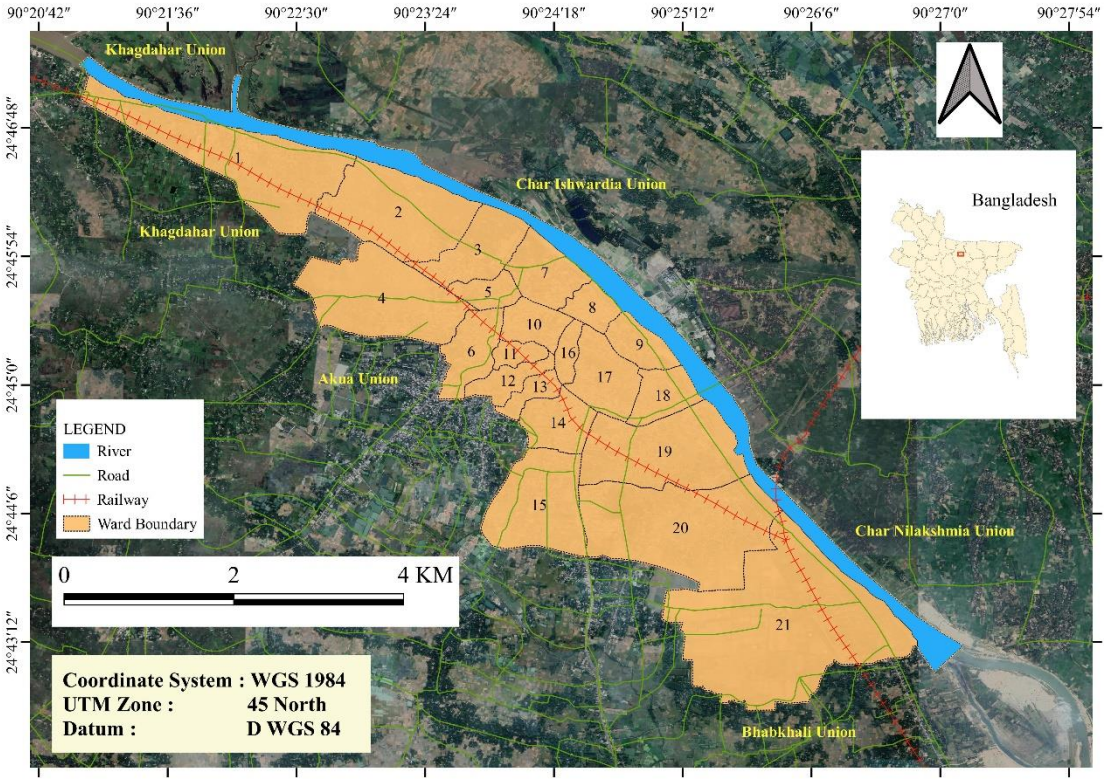

Figure 1. Map of Mymensingh City (Data source: Ward boundary is redrawn from Kabir, 2015)

2.2 Satellite image preprocessing

The necessary data was taken from Landsat satellite images (1989, 2004, and 2019) acquired from the United States Geological Survey's (USGS) database to detect LULC and LST changes. The study area belongs to Landsat path 137 and row 43. All three images were selected from the dry season to avoid cloud cover disturbance. The images were created using the Universal Transverse Mercator (UTM) Zone 45 North projection and the World Geodetic System (WGS) 1984 datum. There is no need for additional rectification or picture correction as part of pre-processing because the images are level-one terrain-corrected (L1T) products (Ahmed et al., 2013; Bonafoni et al., 2016; USGS, 2019). The particulars of the selected images are shown in Table 1. Although Sentinel-2 data are available from 2015 with better resolution (10 m), this data has only spectral bands (for LULC), not thermal bands (required to get LST). On the other hand, Landsat data have both spectral and thermal bands. Therefore, this study used Landsat images to maintain data consistency.

Table 1. Satellite acquisition and weather information

Satellite	Date of acquisition	Spectral band resolution	Thermal band resolution	Air temperature (ºC)	Rainfall (mm)	Cloud cover
Landsat 5	20 Nov 1989	30 m	120 m (resampled to 30 m)	26.33 19.81	0	0
	13 Nov 2004			27.77 18.97	0	0
Landsat 8	23 Nov 2019		100 m (resampled to 30 m)	28.96 17.30	0	3.05

Source: USGS (2019) and BMD (2019)

The images' Digital Numbers (DN) were transformed to Top of Atmospheric (TOA) radiance throughout the radiometric correction procedure using Equations (1) and (2) (Chander and Markham, 2003; USGS, 2014). For Landsat-5 TM:

$$L_\lambda = \text{Gain} * \text{DN} + \text{Bias}\ L_\lambda \quad (1)$$
$$\text{Gain} = (L_{max} - L_{min})/\ Q_{cal}$$
$$\text{Bias} = L_{min}$$

Where; L_{max} represents the spectral radiance scaled to the maximum quantized calibrated pixel value (in W/(m^2*sr*µm)), L_{min} represents the spectral radiance scaled to the minimum quantized calibrated pixel value (in W/(m^2*sr*µm)) and Q_{cal} represents the quantized and calibrated pixel DN. For Landsat-8 OLI:

$$L_\lambda = M_L\ Q_{cal} + A_L \quad (2)$$

Here, M_L is the image metadata-derived band-specific multiplicative rescaling factor, A_L is the image metadata-derived band- specific additive rescaling factor, and Q_{cal} is the quantized and calibrated pixel DN. The photos were free of haze and cloud disruption during the atmospheric correction phase. As a result, no atmospheric adjustment was required.

2.3 LULC mapping by spectral bands

Land use refers to the functional role of humans and their environment, whereas land cover refers to the physical appearances of the earth's surface as represented in the distribution of plants, water, and soil (Kayet et al., 2016). The LULC categories were adapted from the established classification schemes (Anderson et al., 1976; Ahmed et al., 2013; Corner et al., 2014) and shown in Table 2. Firstly, all the spectral bands have been stacked or merged to classify LULC. Each band of a multispectral satellite image traces a feature. The band combination of different bands in a sequence of RGB helps distinguish different land surface features. Different band combinations proposed by Butler (2013) were used, shown in Table 3, as the adjustment of different spectral band combinations has been proved efficient to select suitable training site samples for different LULC categories (Erener, 2013). Landsat images from 1989, 2004, and 2019 were classified into four LULC classes employing supervised classification using the Maximum Likelihood Classifier (MLC) approach (Table 2). The accuracies of LULC maps were evaluated through 200 (50 for each category) ground truth points from Mymensingh Strategic Development (MSDP) base map, Toposheet, and Google Earth images (Corner et al., 2014; Kabir, 2015). These 200 points were selected using a stratified random sampling process. Finally, the confusion matrix of each year was calculated for accuracy assessment to evaluate the level of acceptance (Table 4) (Roy et al., 2015; Roy and Mahmood, 2016).

Table 2. Details of LULC categories

LULC Category	Description
Built-up	Residential, commercial and industrial services, transportation network
Vegetation	Semi-evergreen forest, homestead vegetation, mixed forest, parks and playgrounds, grassland, vegetated lands, agricultural lands, and crop fields.
Bare soil	Vacant land, open space, sand, sand bar, and landfill sites
Water body	Streams, lakes, ponds, rivers, wetlands, and reservoirs.

Source: Adapted from Anderson et al. (1976) and Ahmed et al. (2013)

Table 3. Spectral Band Combination for Landsat OLI 8 and Landsat TM 5 (modified)

Display	Spectral band combination	
	Landsat TM 5	Landsat OLI 8
Natural color	3 2 1	4 3 2
Urban	7 5 3	7 6 4
Vegetation	4 3 2	5 4 3
Agriculture	5 4 1	6 5 2
Vegetation analysis	5 4 3	6 5 4

Source: Butler (2013)

2.4 Extraction of biophysical indices

Six biophysical indices were employed to investigate a statistical relationship between LULC and LST in the study area. The indices include Urban Index (UI), Bare Soil Index (BI), Normalized Difference Builtup Index (NDBI), Normalized Difference Bareness Index (NDBaI), Normalized Difference Vegetation Index (NDVI), and Modified Normalized Difference Water Index (MNDWI) (Ahmed et al., 2013; Dewan and Corner, 2014a; Kafy et al., 2020; Maduako et al., 2016; Rahman et al., 2017; Roy et al., 2020; Ullah et al., 2019). Each index has a value ranging from -1 to +1, with a positive value indicating one land cover feature and a negative value indicating another. All these indices were calculated from the required spectral bands of the images (Table 5).

Table 4. LULC classification accuracy assessment (1989, 2004, and 2019)

Year	User's accuracy (%)				Producer's accuracy (%)				Overall classification accuracy (%)	Overall Kappa Statistics
	Built-up	Vegetation	Bare soil	Water body	Built-up	Vegetation	Bare soil	Water body		
1989	76.32	84.85	87.10	90.63	80.56	88.42	67.50	100.00	84.50	0.7709
2004	84.75	96.72	83.02	96.30	98.04	83.10	95.65	81.25	89.50	0.8569
2019	92.05	87.30	91.67	96.00	96.43	88.71	75.86	96.00	91.00	0.8685

Table 5. Different biophysical indices to relate with LST

Index	Equation	Reference
Urban Index	$\frac{(SWIR2 - NIR)}{(SWIR2 + NIR)}$	Ullah et al. (2019)
Bare Soil Index	$\frac{(SWIR1 + Red) - (NIR + Blue)}{(SWIR1 + Red) + (NIR + Blue)}$	Roy et al. (1997)
Normalized Difference Builtup Index	$\frac{(SWIR1 - NIR)}{(SWIR1 + NIR)}$	Zha et al. (2003)
Normalized Difference Bareness Index	$\frac{(SWIR1 - TIRS)}{(SWIR1 + TIRS)}$	Chen et al. (2006)
Normalized Difference Vegetation Index	$\frac{(NIR - Red)}{(NIR + Red)}$	Chen et al. (2006)
Modified Normalized Difference Water Index	$\frac{(Green - SWIR1)}{(Green + SWIR1)}$	Han-Qiu (2005)

2.5 Derivation of LST

Several techniques have been developed to estimate LST from the thermal band of a satellite image. For example, the Mono-window algorithm (Qin et al., 2001), single-channel algorithm (Sobrino et al., 2004), and split-window algorithm (Jiménez-Muñoz et al., 2014). All of these methods require land surface emissivity (LSE), which varies greatly depending on the thermal emissivity of the surface feature (Sobrino et al., 2004). This study utilized the mono-window approach to calculate LST from the Landsat-5 thermal band between 1989 and 2004. On the other hand, the split-window technique was used to obtain LST from the Landsat-8 thermal band for the year 2019. Landsat sensors record pixel data as digital numbers since the satellite image consists of many pixels for both spectral and thermal bands (DNs) (Chander et al., 2009). This section detailed the steps involved in converting DNs to LST for Landsat-5 and Landsat-8 thermal photos.

The DNs of band-6 were converted to TOA spectral radiance (L_λ) using Equation (3) to estimate LST from Landsat 5 thermal band.

$$L_\lambda = \left(\frac{LMAX_\lambda - LMIN_\lambda}{Q_{calmax} - Q_{calmin}}\right)(Q_{cal} - Q_{calmin}) + LMIN_\lambda \quad (3)$$

Here; L_λ=Spectral Radiance at the Sensor's Aperture [W/m^2 sr μm]; Q_{cal}=Quantized Calibrated

Pixel Value; Q_{calmin}=Minimum Quantized Calibrated Pixel Value Corresponding to $LMIN_\lambda$ [DN]; Q_{calmax}=Maximum Quantized Calibrated Pixel Value Corresponding to $LMAX_\lambda$ [DN]; LMINλ=Spectral at-sensor Radiance that is Scaled to Q_{calmin}; LMAXλ=Spectral at-sensor Radiance that is Scaled to Q_{calmax} (Chander et al., 2009).

Bands 10 and 11 on Landsat 8 are two thermal bands. Each thermal band data of Landsat 8 was converted to TOA spectral radiance (L_λ) using Equation (4) (Zanter, 2015).

$$L_\lambda = M_L Q_{cal} + A_L \quad (4)$$

Here; L_λ=Spectral Radiance at the Sensor's Aperture [W/m^2 sr µm]; M_L=Band-specific multiplicative rescaling factor from the metadata; A_L=Band-specific additive rescaling factor from the metadata; Q_{cal}=Quantized and calibrated standard product pixel values (DN) (Zanter, 2015).

Then, the spectral radiance (L_λ) of both Landsat 5 and 8 were transformed to at-sensor brightness temperature (T_B) by Equation (5).

$$T_B = \frac{K_2}{\ln\left(\frac{K_1}{L_\lambda}+1\right)} \quad (5)$$

Here; K_1 and K_2 are thermal conversion constants in W/m^2 sr µm and Kelvin units (K) of the TIR band (Chander and Markham, 2003).

The difference in Land Surface Emissivity (LSE) due to surface wetness, features, roughness, and viewing angle is critical for LST derivation (Salisbury and Aria, 1994). The LSE was estimated by Equation (6) (Avdan and Jovanovska, 2016; Pal and Ziaul, 2017; Roy et al., 2014).

$$LSE\ (\varepsilon) = 0.004 * P_v + 0.986 \quad (6)$$

The NDVI threshold is the most appropriate approach of emissivity extraction among numerous options because of its ease in the estimate (Van de Griend and Owe, 1993; Sobrino and Raissouni, 2000). P_v is the Proportion of Vegetation calculated from Equation (7) (Roy et al., 2014; Yu et al., 2014).

$$P_v = \left(\frac{NDVI - NDVI_{min}}{NDVI_{max} - NDVI_{min}}\right)^2 \quad (7)$$

For Landsat-5, LST in Degree Celsius (ºC) was derived by Equation (8) (Artis and Carnahan, 1982; Roy et al., 2014; Yu et al., 2014).

$$LST = \frac{T_B}{\left\{1+\left(\frac{\lambda T_B}{\rho}\right)\ln LSE\right\}} - 273.15 \quad (8)$$

Here; λ=wavelength of emitted radiance in meters (for which the peak response and the average of the limiting wavelengths, λ=1.5 µm) (Markham and Barker, 1985) is used; ρ=h*c/σ (1.438×10^{-2} mK); σ (Boltzmann constant)=1.38×10^{-23} J/K; h (Planck's constant)=6.626×10^{-34} Js and c (velocity of light) =2.998×10^{8} m/s (Roy et al., 2014; Scarano and Sobrino, 2015).

The split-window approach was used to calculate LST from Landsat-8 TIRS pictures, which is described by Equation (9) (Gazi et al., 2020; Roy et al., 2020). TIRS bands of Landsat 8 are different from the TM band of Landsat 5. Previous TM sensor is the presence of two TIR bands in the atmospheric window between 10 and 12 µm. Nevertheless, TIRS bands are narrower than the previous TM band. Here, split-window (SW) algorithms are applied to TIR bands instead of mono-window or single-channel (SC) algorithms for LST retrieval (Jiménez-Muñoz et al., 2014).

$$T_s(K) = T_{10} + C_1(T_{10} - T_{11}) + C_2(T_{10} - T_{11})^2 + C_0 + (C_3 + C_4 w)(1-\varepsilon) + (C_5 + C_6 w)\Delta\varepsilon \quad (9)$$

Here; T_{10} and T_{11} are at-sensor brightness temperatures of TIRS bands (in K). T_{10} and T_{11} have been calculated from Equation (3). C_0-C_6 are coefficients (Jiménez-Muñoz et al., 2014), ε represents the mean surface emissivity, Δε represents emissivity difference, and w represents the atmospheric water vapor content (in gm cm^{-2}) acquired from the Atmospheric Correction Parameter Calculator developed by NASA (2019). The values of LST of Landsat-8 were converted to Degree Celsius (ºC) unit by subtracting 273.15 from Equation (9).

2.6 Simulation of future LULC

The Multilayer Perceptron (MLP) model addresses the trend of LULC changes (e.g., growth) in developed areas by automatically producing network parameter decisions for better modeling (Veronez et al., 2006). After recognizing a pattern, it analyses the input and generates a random high-accuracy output. One appealing feature of this model is that it allows simulating many or even all of the transitions at once. The MLP neural network uses the Back Propagation (BP) technique. MLP-MC works with one or more layers between input and output

through a feed-forward Neural Network (Ahmed and Ahmed, 2012; Kafy et al., 2020). This modeling is applied to simulate future LULC maps in IDRISI Selva v17 software. The model considers large and small LULC change causes and evaluates future prediction models based on their accuracy (Ahmed and Ahmed, 2012; Mishra and Rai, 2016; Kafy et al., 2020).

The change in LULC is not confined to a single component; instead, it has both natural and artificial factors and determinants. A composition of dependent and independent variables is used to predict LULC change. The study's dependent variables were DEM, slope, aspect, distance from main roads, and distance from built-up regions, while the independent variables were LULC maps in 2004 and 2019 (Figure 2(b) and 2(c)) (Kafy et al., 2020). The SRTM-DEM was used to derive elevation, slope, and aspect using QGIS v.2.8 software. The distance to main roads and built-up regions, on the other hand, was computed using vector layers from the Open Street Map (OSM) (Kafy et al., 2020).

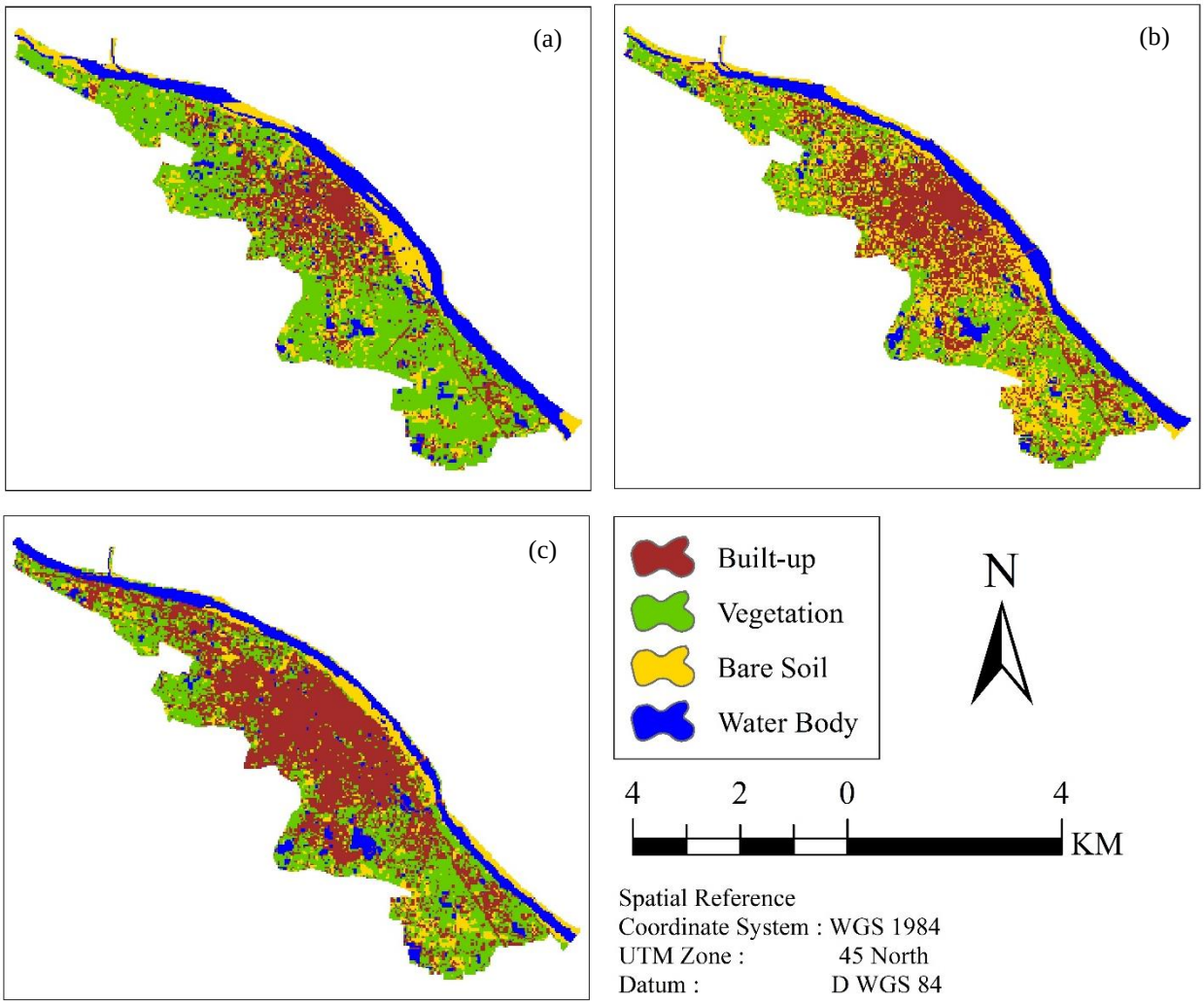

Figure 2. Land Use Land Cover maps of different years: (a) 1989, (b) 2004, and (c) 2019

All the variables mentioned above were added as processing parameters to get the potentiality of the transformation matrix. The expected matrix analysis generates the change probability of different LULC categories. After generating the potential transformation matrix, the prediction model has been run to simulate the LULC map of 2034. As a part of the model assessment, validation was performed using the existing database (Kafy et al., 2020). It was executed by cross-checking between simulated and existing LULC maps of the year 2019. As a part of the validation, some parameters (Kappa) were produced, including $K_{location}$, K_{no}, $K_{locationStrata}$, and $K_{standard}$ (Kafy et al., 2020; Mishra et al., 2018).

2.7 Simulation of future LST

The Artificial Neural Network (ANN) was proved effective for predicting LST by some previous studies (Kafy et al., 2020, Maduako et al., 2016). It is a machine learning algorithm that simulates future LST as an output layer using input, hidden layers (Li et al., 2013; Maduako et al., 2016). It was developed to predict the LST for the year 2034. The input layers were chosen based on the relation between LST and LULC since this model required input layers (Ahmed et al., 2013; Kafy et al., 2020; Rahman et al., 2017; Ullah et al., 2019). Initially, LST variations for different LULC categories were evaluated each year (1989, 2004, and 2019). Then a bivariate correlation investigation was performed between each LULC index (e.g., UI) and LST to examine the relationship strength. Here LST was regarded as a dependent variable, and indices were regarded as independent variables. Highly correlated indices were selected as input layers in the ANN model with LULC types. The ANN model was developed using the neuralnet package of R software. Accuracy assessment of the ANN model was also done using training and testing data (Kafy et al., 2020; Maduako et al., 2016). Detail description of this section is given later.

3. RESULTS

As mentioned in the methodology (in section 2), this section intends to discuss the Spatio-temporal changes in the distribution of LULC and LST and the simulation of the future LULC and LST maps.

3.1 Changes in Land Use Land Cover

Supervised classification through maximum likelihood estimation was applied using Landsat images' spectral bands to detect the change of LULC (1989-2019) patterns (Figure 2). The error matrix of this supervised classification showed an overall accuracy of 84.50, 89.50, and 91.00% in the years 1989, 2004, and 2019, respectively (Table 4).

Two trends in the changes of LULC have appeared in the findings (Figure 2 and Figure 3), such as (i) a continuous increase of built-up area and decrease of the water body; and (ii) an increase of bare soil between the first two periods, then decrease towards the third period. More specifically, built-up has become dominating land cover type in 2019, as it increased more than two times (578.50 ha) in the past 30 years (Figure 3, Table 6). The overall increase is 24.99%. Migration from rural to urban areas has resulted in population expansion, which is the main force behind the expansion in the built-up area. The built-up area's spatial growth pattern demonstrates substantial expansion in the South-East (SE) and North-West (NW) directions. In 2004, the growth towards the SE direction was 224.91 ha, which became 328.77 ha in 2019. In the case of growth towards NW direction, it was 158.58 ha in 2004 and increased to 277.02 ha in 2019 (Figure 4).

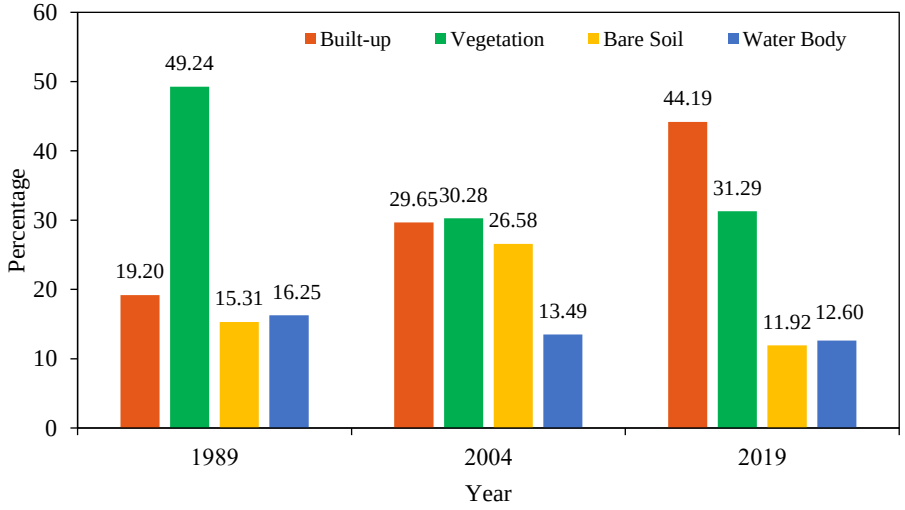

Figure 3. Percentages of LULC types in Mymensingh City (1989-2019)

The vegetation cover dominated the land cover category (1140.48 ha) in 1989, which experienced a reduction of about 415 ha by 2019. The Overall decrease in vegetation cover is 17.95% (415.80 ha) from 1989 to 2019 (Figure 3, Table 6). Bare soil was increased (261.09 ha) only up to 2004 and is decreased

339.48 ha from 2004 to 2019 (Table 6). Although bare soil fluctuated by showing both increases and decrease throughout the change, the overall decrease is 78.39 ha compared to the area in the first year to the area last year (3.38%) (Figure 3, Table 6). Among all the land cover types, the only water body has experienced a gradual decrease of 84.51 ha (3.65%) in the last three decades (Table 6).

The transition matrix is a sophisticated method to study LULC change in more detail, and it calculates the amount of inter-conversion between different forms of land cover. The results in Table 7 demonstrate that the Built-up area has gained land cover from vegetation (379.80 ha) and bare soil area (102.33 ha). Similarly, vegetation cover has also expanded by obtaining area from bare soil and water body. Besides, the bare soil has grown by gaining its maximum area from vegetation cover (91.08 ha), followed by the water body (82.98 ha). The transition matrix revealed that the vegetation and water body had been converted into bare soil, then the bare soil was quickly changed to a built-up area. In the same way, bare soil and water body have been transformed into vegetation cover. Also, significant portions of bare soil and water body are located in the adjacent river channel as sand bars and running water.

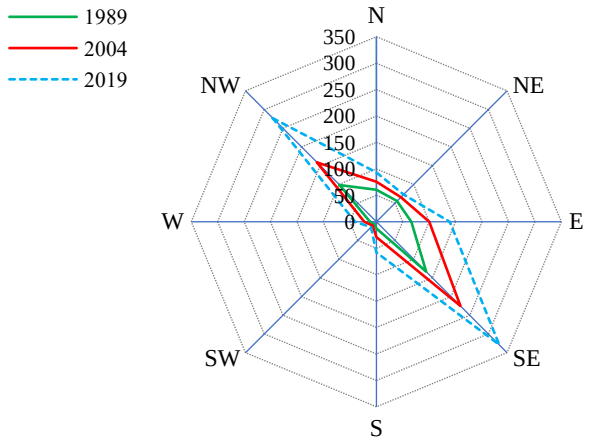

Figure 4. Spatial-temporal growth patterns of built-up area in 8 directions (in ha)

Table 6. LULC changes from 1989 to 2019

LULC Type	1989-2004		2004-2019		1989-2019	
	Area (in ha)	%	Area (in ha)	%	Area (in ha)	%
Built-up	242.10	10.45	336.60	14.53	578.70	24.99
Vegetation	-439.20	-18.96	23.40	1.01	-415.80	-17.95
Bare soil	261.09	11.27	-339.48	-14.66	-78.39	-3.38
Water body	-63.99	-2.76	-20.52	-0.89	-84.51	-3.65

Table 7. Transition matrix between LULC categories (1989-2019)

Conversion		Area (in ha)
Unchanged built-up		484.56
Vegetation	Built-up	379.80
	Unchanged	691.83
	Bare soil	91.08
	Water body	28.17
Bare soil	Built-up	102.33
	Vegetation	64.44
	Unchanged	57.24
	Water body	49.77
Water body	Built-up	22.50
	Vegetation	22.77
	Bare soil	82.98
	Unchanged	216.81

3.2 Changes in land surface temperature

The Spatio-temporal distribution of LST for 1989, 2004, and 2019 was calculated using thermal bands from Landsat data employing multiple techniques (section 2.5). The categorization of LST is helpful to get distribution in the area unit of different temperature ranges (Ahmed et al., 2013; Kafy et al., 2020). This study found that the temperature varies from 20 to 35ºC, which was then classified into seven ranges (<21ºC, 21ºC to <23ºC, 23ºC to <25ºC, 25ºC to <27ºC, 27ºC to <29ºC, 29ºC to <31ºC and ≥31ºC). The spatial distribution of LST in different years is shown in Figure 5.

Different ranges of LST were found, such as 20.90ºC-26.41ºC, 22.52ºC-29.71ºC and 24.71ºC-34.42ºC, during the years of 1989, 2004, and 2019, respectively (Figure 5). In 1989, no regions had temperatures below 27ºC, and the highest temperature coverage was below 23ºC, as shown in Table 7. In 2004, the majority temperature zone shifted to 23-25ºC (55.45%), which shows an overall increase of higher temperature zones. This upward trend continued in 2019, with a considerable portion of

the study region (55.73%) shifting to higher temperature zones (27 to 29ºC). In 2019, no area remained in the lower temperature zones, which is noteworthy (Table 8).

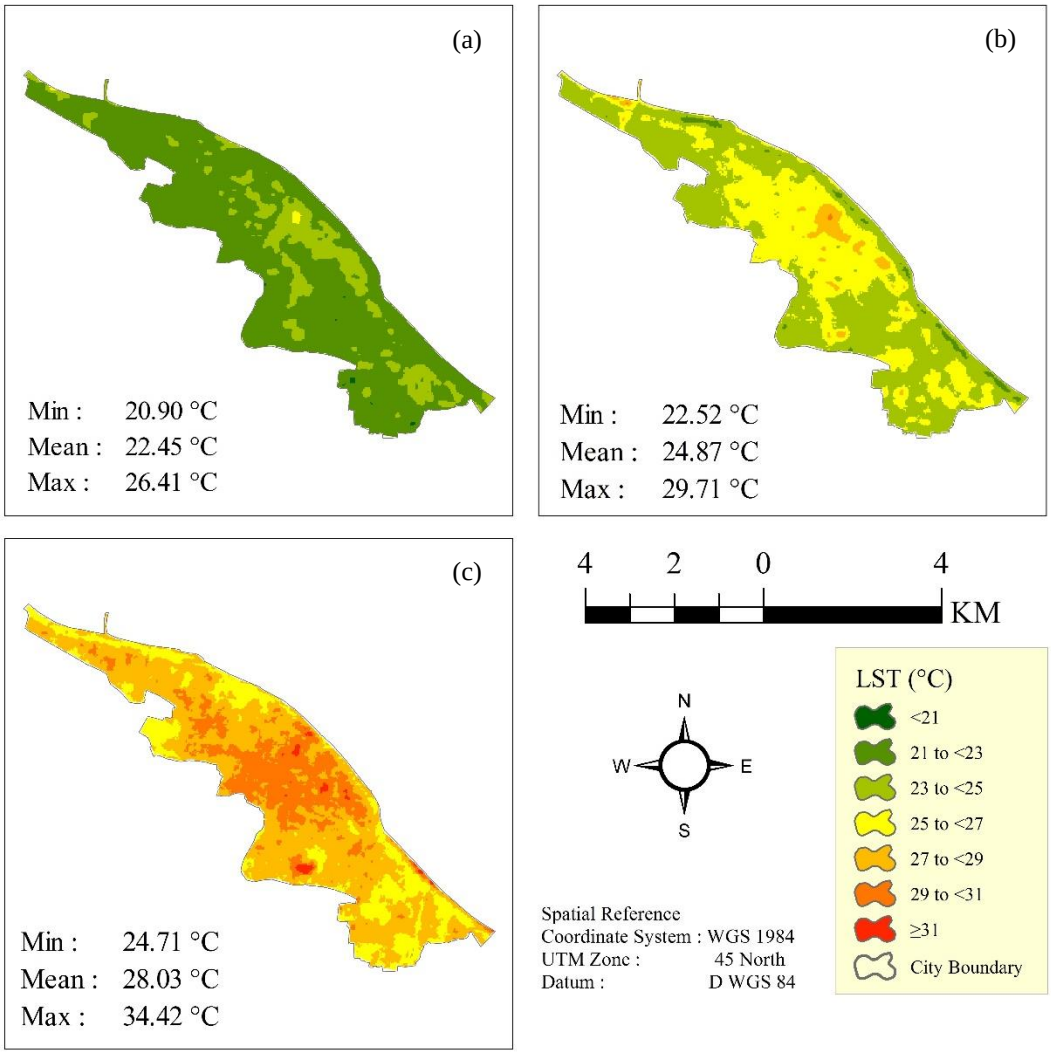

Figure 5. Spatial distribution of LST (1989-2019): (a) 1989, (b) 2004, and (c) 2019

Table 8. Distribution of LST amongst different classes (1989, 2004, and 2019)

Ranges of LST (ºC)	1989		2004		2019	
	Area	%	Area	%	Area	%
<21ºC	3.24	0.14	-	-	-	-
21 to <23ºC	1881.45	81.23	37.17	1.60	-	-
23 to <25ºC	395.55	17.08	1284.21	55.45	0.45	0.02
25 to <27ºC	5.94	0.26	887.40	38.32	484.56	20.92
27 to <29ºC	-	-	76.14	3.29	1290.78	55.73
29 to <31ºC	-	-	1.26	0.05	492.12	21.25
≥31ºC	-	-	-	-	18.27	0.79
Total	2316.06	100.00	2316.06	100.00	2316.06	100.00

3.3 Validation of LST data

Validation of calculated LST using in-situ measurements or any other satellite sensor is required to determine the correctness of LST data (Guha et al., 2019; Gazi et al., 2020). MODIS Terra data sets were used as a reference image in this research to validate LST values. The MODIS data are available from 2,000, and the MOD11A1 data with a spatial

resolution of 1,000 m acquired during the same periods were used to validate the observed LST data. In order to integrate with Landsat LST, 1,000-m pixel size was resampled into 30-m pixel size (Guha et al., 2019). A total of 100 random points has been selected to correlate LST from the Landsat image with the MODIS image for 2004 and 2019. For the following reasons, there is some difference between the LST obtained from Landsat data sets and the respective MODIS data sets: (a) There is a 30 minutes interval between the Landsat sensors and MODIS sensors; (b) water vapor content; and (c) technique of resampling (Huete et al., 2010). Despite this, a moderately strong correlation has been observed between the calculated LST from Landsat data sets and MODIS data sets in 2019 and 2004 without any pre-processing (Figure 6).

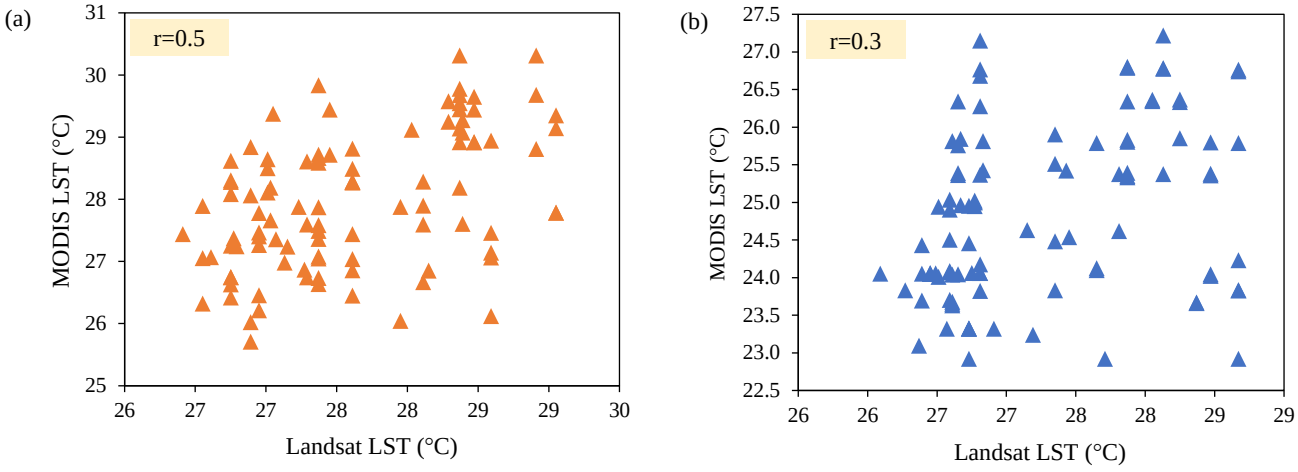

Figure 6. Validation of LST: (a) 2019 and (b) 2004

3.4 Relation between LULC and LST

Two approaches were applied to relate LULC with LST. The first one is zonal statistics between LULC categories and LST to assess variations of LST for each land cover type (Weng, 2001). Secondly, a correlation between biophysical indices and the LST of each year (Ahmed et al., 2013; Kafy et al., 2020; Rahman et al., 2017; Ullah et al., 2019).

For each land cover category, zonal statistics show the maximum, minimum, and average distribution of LST. Figure 7 shows the LST distribution with pixel numbers/frequency by LULC category of all three periods. In all three sampling periods, the built-up area has the highest LST compared to other LULC categories. The findings show that built-up regions have raised surface temperatures by replacing natural vegetation and water bodies with heat-prone, low-albedo, non-evaporating, and non-transpiring surfaces. Similarly, bare soil has higher LST in all parameters after the built-up category. On the contrary, both vegetation and water body have lower LST. For three decades, the overall LST of each land cover has been increased gradually with an average value of 5.75ºC, 5.27ºC, 5.31ºC, and 4.91ºC for built-up, vegetation, bare soil, and water body category, respectively. These data support the urban warming hypothesis; otherwise, natural LULC like plants and water bodies would not have experienced an increase in temperature. Similar urban micro-climatic warming scenarios were reported in other cities like Dhaka, Chattogram, and Rajshahi (Ahmed et al., 2013; Gazi et al., 2020; Kafy et al., 2020; Roy et al., 2020). The total LST of other surrounding land covers increased due to this gradual increase in warm land cover types, such as built-up and bare soil (Figure 7).

The correlation approach was used to quantify the strength of the associations between land cover indices and LST. The LST was correlated with each of the indices individually (Table 6). Among the indices, the UI and NDBI represent the built-up area; the BI and NDBaI belong to bare soil; and the NDVI and MNDWI represent vegetation and water body, respectively. Figure 8 shows both positive and negative correlations between biophysical indices and LST. According to the findings, the LST appears to be positively connected with UI, BI, NDBI, and NDBaI. NDVI and MNDWI, on the other hand, have a negative association. In the case of higher positive correlation, UI and BI were found suitable in each year (r>0.6) (Figure 8(a) and 8(b)). Among natural biophysical indices, the MNDWI, rather than the

NDVI, exhibited a strong negative connection (r<-0.25) with LST in each year (Ahmed et al., 2013; Kafy et al., 2020; Roy et al., 2020). In short, the UI, BI, and MNDWI values were found as significant determinants of LST as per the correlation test results. This research also revealed that the replacement of natural land cover by built-up and bare soil over long periods resulted in significant urban warming. On the other hand, the vegetation and water bodies exhibited lower LST as a natural land cover category (Figure 7 and Figure 8).

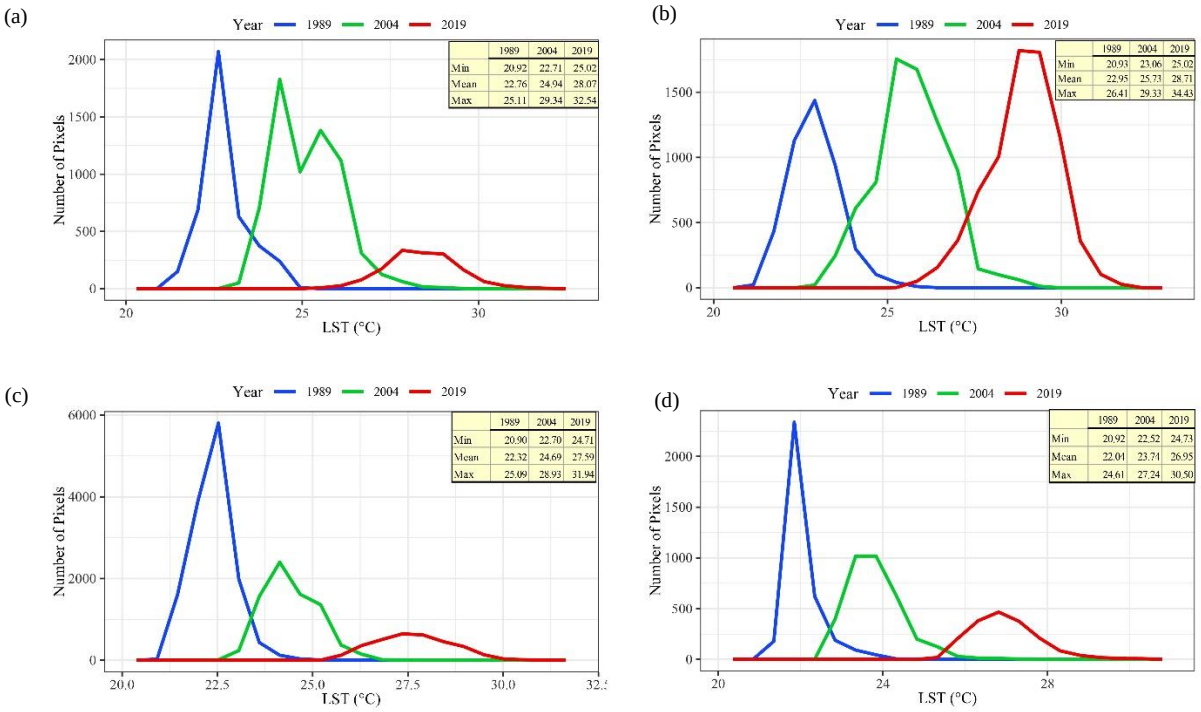

Figure 7. Variations of LST over different LULC types: (a) Bare soil, (b) Built-up, (c) Vegetation, and (d) Water body

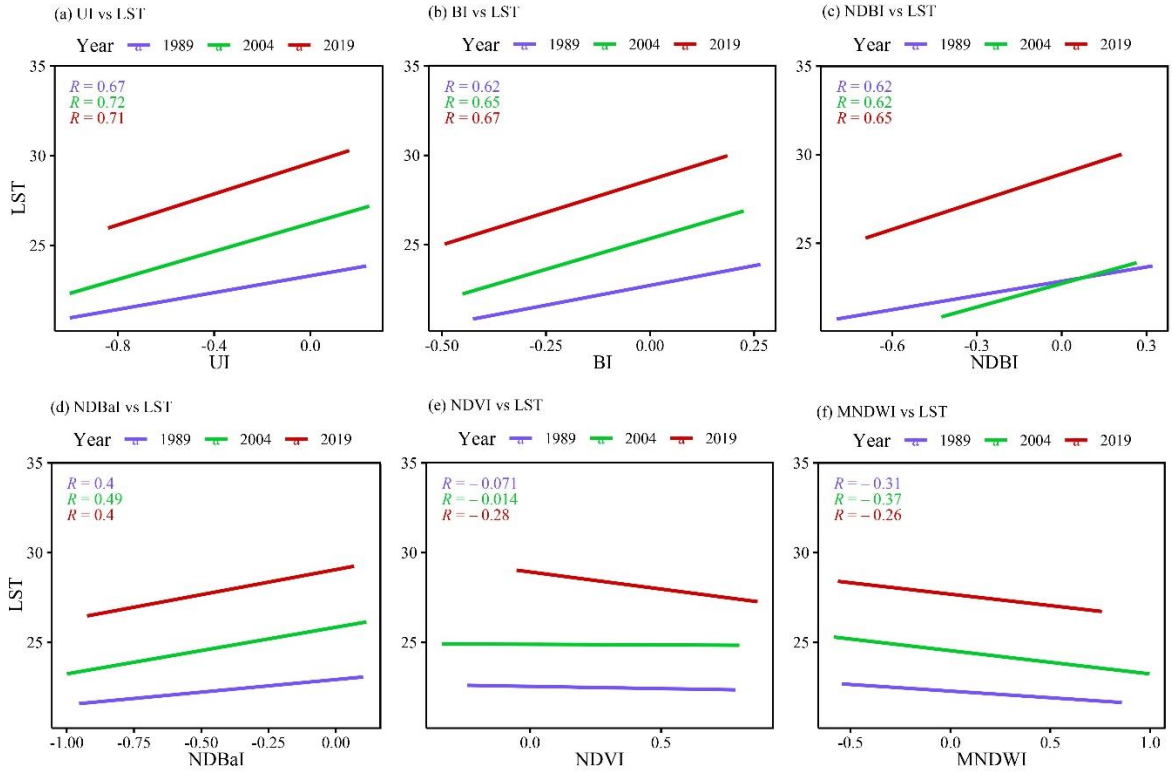

Figure 8. Correlation between biophysical indices [(a) UI, (b) BI, (c) NDBI, (d) NDBaI, (e) NDVI, and (f) MNDWI] and LST

3.5 Simulating the future LULC

The simulation of the future LULC of Mymensingh city is one of the objectives of this research. The MLP-MC Model was used to model the likely LULC scenario of 2034 using LULC maps from 2004 and 2019 (Ahmed and Ahmed, 2012; Corner et al., 2014; Kafy et al., 2020). The LULC simulation of the year 2019 was done as indicated in section 2.6 to get a valid LULC forecast for the year 2034 by MLP-MC. Kappa index statistics were used to test the correctness of the MLP-MC Model as part of the validation component. The statistics show that K_{no}, $K_{location}$, $K_{locationStrata}$, and $K_{standard}$ values were 0.8494, 0.7892, 0.7892, and 0.7240 (overall kappa), respectively. This model was utilized for LULC prediction after successful validation. A transition probability matrix was created by cross-tabulating two LULC maps from 2004 and 2019 in the MLP-MC analysis (Table 9).

According to the simulation results, in 2034, about 59.42 percent of the study area will be turned into a "built-up area" land cover type (Figure 9).

Table 10 shows the overall change statistics between observed land cover (in 1989 and 2019) and simulated land cover (in 2034). The built-up area will expand by 40.22 percent between 1989 and 2034, whereas vegetation, bare soil, and water body area will decline by 29.48 percent, 8.61 percent, and 2.13 percent, respectively. On the other hand, according to the 2019-2034 time-span, the built-up and water body category area will be increased by 15.23% and 1.52%, respectively. In contrast, the vegetation and bare soil area will be decreased by 11.53% and 5.22%, respectively. Although some portions of the water body will remain unchanged, the close or stagnant water bodies are more vulnerable to decrease than the river or running water body.

Table 9. Probability of LULC transformation change matrix (2004-2019) for 2034

	Built-up	Vegetation	Bare soil	Water body
Built-up	0.9921	0.0021	0.007	0.004
Vegetation	0.3247	0.522	0.1006	0.0527
Bare soil	0.4723	0.3264	0.1032	0.0982
Water body	0.1463	0.1627	0.2243	0.4668

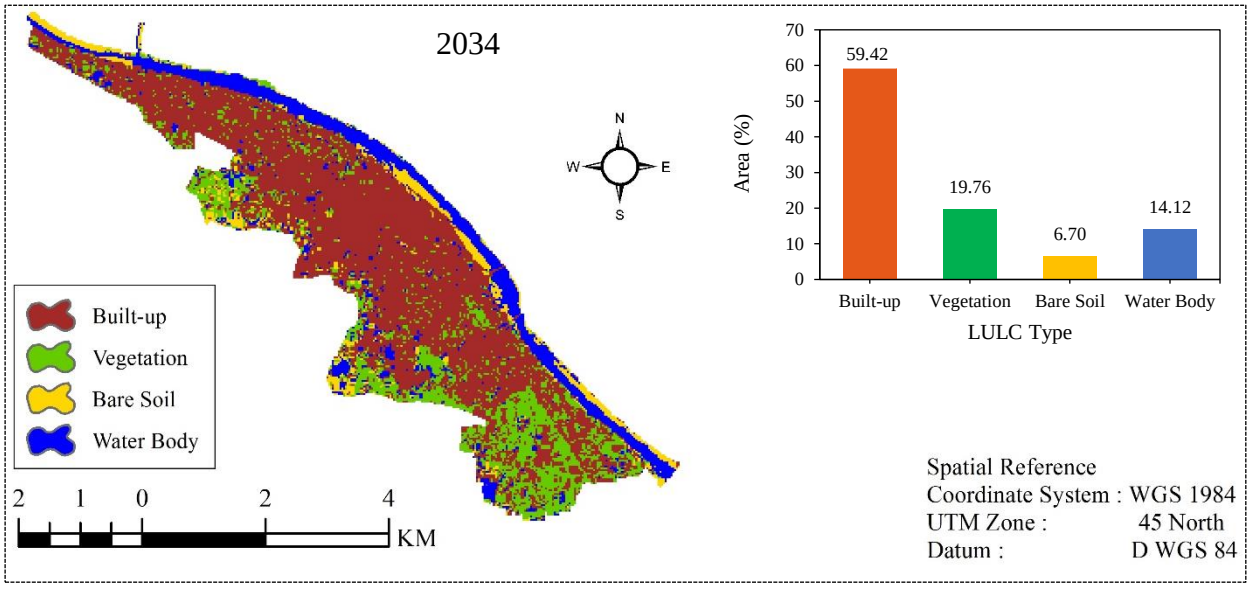

Figure 9. MLP-MC model simulated land cover map of Mymensingh city in 2034

Table 10. LULC statistics for the predicted year 2034

LULC Type	1989		2019		2034		Change (1989-2034)		Change (2019-2034)	
	Area	%	Area	%	Area	%	Area	%	Area	%
Built-up	444.69	19.20	1023.39	44.19	1376.10	59.42	931.41	40.22	352.71	15.23
Vegetation	1140.48	49.24	724.68	31.29	457.74	19.76	-682.74	-29.48	-266.94	-11.53
Bare soil	354.51	15.31	276.12	11.92	155.16	6.70	-199.35	-8.61	-120.96	-5.22
Water body	376.38	16.25	291.87	12.60	327.06	14.12	-49.32	-2.13	35.19	1.52

3.6 Simulation of LST for the year 2034

In ANN Model, the highly correlated biophysical indices like UI, BI, and MNDWI were taken as input layers with LULC types for the LST simulation process (Figure 8) (Kafy et al., 2020; Maduako et al., 2016). Since the ANN model requires training and testing data to construct a model and simulate, 2004 and 2019 were taken as training and testing data. Figure 10 shows the structure of the ANN model, having four input layers, three hidden layers, and predicted LST as the output layer.

The investigation indicated a considerable change in LST during a three-decade period, similar to the LULC change analysis. Therefore, the LST was simulated for the future year 2034. The predicted LST of 2034 shows that the LST will be increased by almost 8ºC from 1989 and 2ºC from 2019 on average (Figure 11). LST will exceed 29ºC in the majority of the city (59.64%). After that, 23.55% of the study area will have LST above 31ºC, and there will be no area below 25ºC LST.

To cross-validate, both simulated LST and LULC, the zonal statistics were calculated to assess LST variations over LULC (Figure 12(a)). The findings show that the built-up land use will have the highest LST (average, maximum) because of the increased built-up area found in the LULC prediction (Figure 12(a), Table 10). Although vegetation and water body tend to lower LST, the urban warming effect caused by increasing built-up areas will exaggerate the LST of vegetation and water body. Among all the LULC-LST distribution curves, the built-up and bare soil category will occupy a higher LST zone, whereas the water body category will be in the lower LST zone compared to the vegetation category (Figure 12(a)). Compared to all years' LST distribution curves, the simulated LST curve will move to a higher temperature zone (Figure 12(b)). As with LULC, the LST simulation model was also validated using a confusion matrix that shows the accuracy of 0.8697 and 0.9034 for training and testing data, respectively, which is a satisfactory level of accuracy for LST simulation.

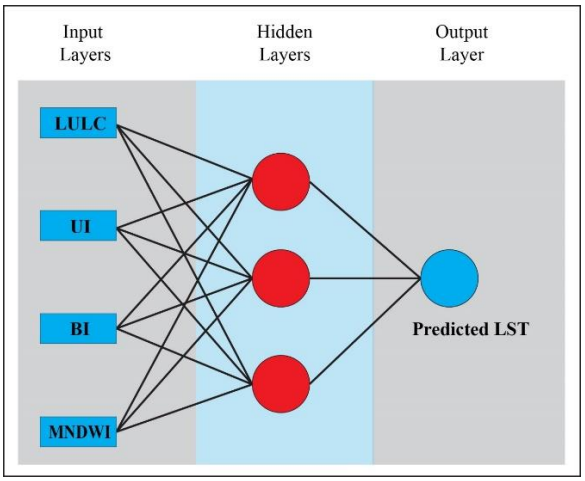

Figure 10. ANN model architecture

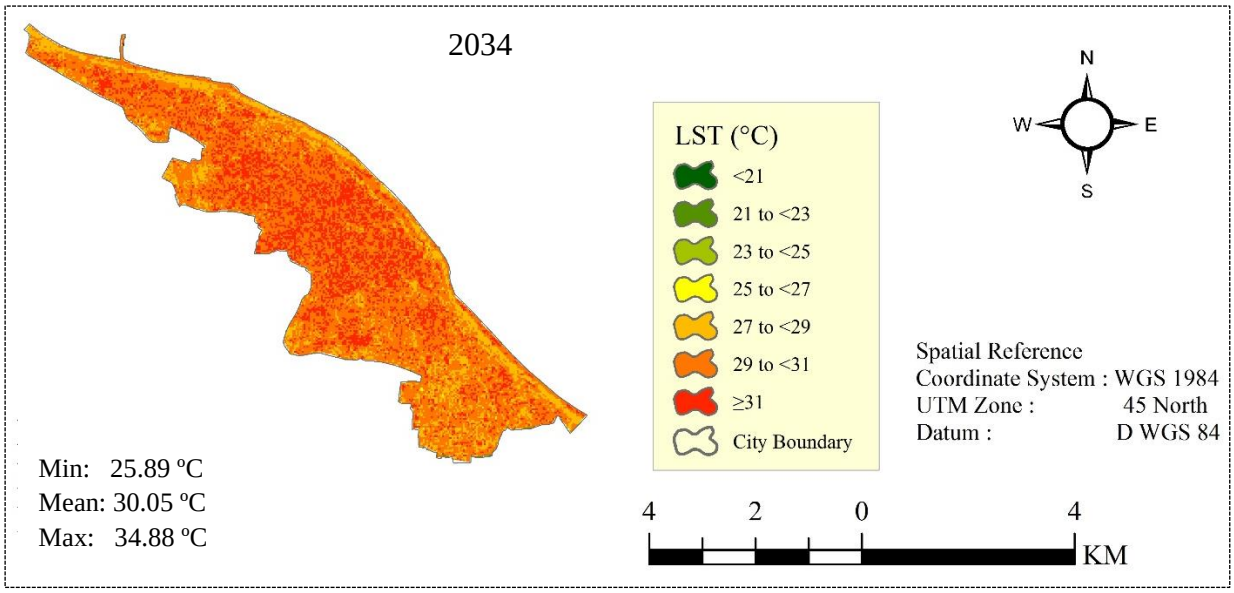

Figure 11. Simulated LST of the year 2034

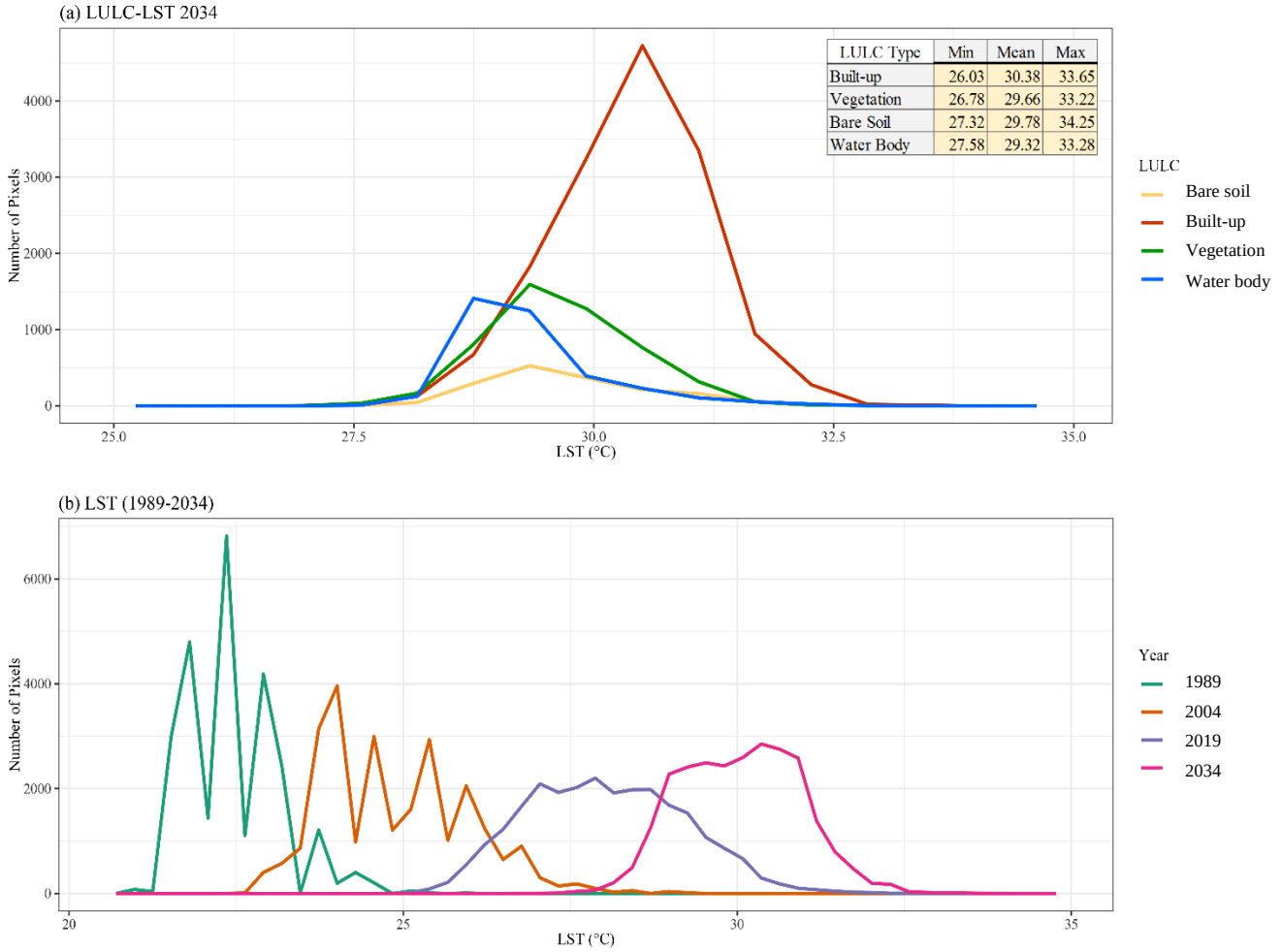

Figure 12. Simulated LST of 2034 (a) Zonal Statistics with predicted LULC 2034 and (b) variations of LST (1989-2034)

4. DISCUSSION

The effects of land cover changes on LST in the Mymensingh city region are modelled in this study for the year 2034. Several studies in Bangladesh have attempted to forecast both LULC and LST (Ahmed et al., 2013; Kafy et al., 2020). At first, both LULC and LST of Mymensingh city were studied for three different years (1989, 2004, and 2019). The MLP-MC model was used to forecast the future LULC in 2034. This study used zonal statistics and correlation to investigate the relationship between LULC and LST over three time periods to simulate LST. For all three periods, the analyzed correlations appeared to be compatible with the primary outputs indicated in the literature, such as (i) greater temperatures were found in built-up and bare soil regions, while lower temperatures were found only in vegetation and water bodies (similar results were found by Ahmed et al. (2013), Dewan and Corner (2014a), Kafy et al. (2020), and Roy et al. (2020)); (ii) correlation analysis showed a positive relation of LST with UI, BI, NDBI, NDBaI; and a negative relation of LST with other two biophysical indices (e.g., NDVI and MNDWI) considered in this study (similar results were also found by Ahmed et al. (2013), Kafy et al. (2020), and Roy et al. (2020)). Three biophysical indices (e.g., UI, BI, and MNDWI) and LULC types were chosen as input layers of the ANN model for LST prediction based on the observed association between LULC and LST. The prediction shows an increasing trend of the built-up category of LULC and temperature for LST on average, which is a sign of the rising effect of UHI in the upcoming future of Mymensingh city. In future predictions for other Bangladeshi cities, such as Dhaka and Rajshahi, a similar tendency to increase built-up area was found (Ahmed et al., 2013; Corner et al., 2014; Kafy et al., 2020). In the case of Bangladesh, rising built-up areas could be linked to both population increase and urbanization (BBS, 2011; Hasan et al., 2017). Urban sprawl caused by rapid urbanization will replace natural land covers like vegetation, bare soil, waterbody, etc., which is also found in the simulation of 2034 (Figure 9; Dewan and Corner, 2014b).

The built-up area has grown as a result of population increase and development. The vegetation cover and water body are low-cost lands that are easy to develop into an urbanized area. The trend of LULC change has been used to simulate future LULC, which revealed a drastic growth of the built-up area as a dominating LULC category. The built-up materials (i.e., solid brick) trap heat from solar radiation, causing the built-up surface to have higher LST. At the same time, anthropogenic heat like energy consumption, fossil fuel burning, etc., causes heat production. Similarly, bare soil also traps heat due to the absence of vegetation or greenery on it. On the other hand, the vegetation balances its body or surface temperature through the process of evapotranspiration (Solecki et al., 2005). The water body has a higher heat transfer capacity, which causes a lowering of its LST. A correlation between LST and biophysical indices has also validated or proved positive relation with built-up and bare soil and negative relation with vegetation and water body. The results show that the rise of the built-up area and the reduction of vegetation and water body area are critical contributors to the net increase in LST. Simulation of LST has shown an increase of LST due to the growth of the built-up area. The urban area has promoted the effect of UHI by decreasing natural land cover, including both terrestrial and aquatic (Li et al., 2012; Xu et al., 2009). The growth of UHI has detrimental consequences for humans, biodiversity, ecology, and the environment (Grimmond, 2007). Moreover, geographic location makes the Asian region face higher temperatures than the earth's average (IPCC, 2014). At the same time, due to global warming, the greenhouse effect, and changes in surface features, LST will rise even in non-urbanized places (Dereczynski et al., 2013; Kafy et al., 2020).

The impact of UHI expansion must be decreased in order to meet the SDGs 11 target of sustainable cities (Rosa, 2017). Recently, the greater Mymensingh district has been classified as a less disaster-prone zone by Bangladesh Delta Plan 2100, which is a positive sign of barrier-free development (Bangladesh Planning Commission, 2017). Therefore, sustainable urban development has to be assured through considering the issues related to LULC and LST change.

5. CONCLUSION

This study was carried out in Mymensingh City to assess changes in LULC and LST from 1989 to 2019. As per the study's objective, the prediction of LULC and LST was performed for the year 2034. The simulation of LULC shows that the vegetation, bare soil, and water body areas will decrease compared to their initial extent in 1989. Similarly, LST will be increased by 7.60ºC on average. More than 29ºC LST will likely be experienced by 83.2% of the total area. The built-up and bare soil LULC categories will have higher LST. It will create health, economic, and environmental problems for the city if this changing rate of LULC and LST goes upwards in the upcoming years. The findings of this study will be instructive for administrators, policymakers, and planners, who can make effective use of these study findings for sustainable development and formulation of a future master plan. Moreover, it is essential to establish rules, regulations, and strategies as a part of environmental conservation to keep LST within a reasonable level in the city. Future researchers may give attention to the microclimatic change in the city from the UHI perspective.

ACKNOWLEDGEMENTS

Authors are thankful to Md. Golam Mortoja for his cordial help in this study.

REFERENCES

Ahmed B, Ahmed R. Modeling urban land cover growth dynamics using multi-temporal satellite images: A case study of Dhaka, Bangladesh. ISPRS International Journal of Geo-Information 2012;1(1):3-31.

Ahmed B, Kamruzzaman MD, Zhu X, Rahman M, Choi K. Simulating land cover changes and their impacts on land surface temperature in Dhaka, Bangladesh. Remote Sensing 2013;5(11):5969-98.

Alam MK, Hasan AK, Khan MR, Whitney JW. Geological Map of Bangladesh [Internet]. 1990 [cited 2020 Mar 3]. Availabe from: https://pubs.usgs.gov/of/1997/ofr-97-470/OF97-470H/ofr97470H_geo.pdf.

Alam MS, Haque SM. Assessment of urban physical seismic vulnerability using the combination of AHP and TOPSIS models: A case study of residential neighborhoods of Mymensingh city, Bangladesh. Journal of Geoscience and Environment Protection 2018;6(2):165-83.

Al-sharif AA, Pradhan B. Monitoring and predicting land use change in Tripoli Metropolitan City using an integrated Markov chain and cellular automata models in GIS. Arabian Journal of Geosciences 2014;7(10):4291-301.

Anderson JR, Hardy EE, Roach JT, Witmer RE. A Land Use and Land Cover Classification System for Use with Remote Sensor Data. USGS Professional Paper 964. Sioux Falls, USA: United States Geological Survey; 1976.

Artis DA, Carnahan WH. Survey of emissivity variability in thermography of urban areas. Remote Sensing of Environment 1982;12(4):313-29.

Avdan U, Jovanovska G. Algorithm for automated mapping of land surface temperature using LANDSAT 8 satellite data. Journal of Sensors 2016;2016:Article No. 1480307.

Bahi H, Rhinane H, Bensalmia A, Fehrenbach U, Scherer D. Effects of urbanization and seasonal cycle on the surface urban heat island patterns in the coastal growing cities: A case study of Casablanca, Morocco. Remote Sensing 2016;8(10): Article No. 829.

Bangladesh Bureau of Statistics (BBS). Population and Housing Census 2011. Dhaka, Bangladesh: Ministry of Planning, Govt. of Bangladesh [Internet]. 2011 [cited 2020 Mar 3]. Available from: http://www.bbs.gov.bd/site/page/47856ad0-7e1c-4aab-bd78-892733bc06eb/Population-and-Housing-Census.

Bangladesh Meteorological Department (BMD). Climate Data Library [Internet]. 2019 [cited 2020 Mar 3]. Available from: http://datalibrary.bmd.gov.bd/maproom/Climatology/index.html.

Bangladesh Planning Commission. Bangladesh Delta Plan 2100. Dhaka, Bangladesh: Ministry of Planning, Govt. of Bangladesh [Internet]. 2017 [cited 2020 Apr 17]. Available from: http://www.plancomm.gov.bd/site/files/0adcee77-2db8-41bf-b36b-657b5ee1efb9/Bangladesh-Delta-Plan-2100.

Bokaie M, Zarkesh MK, Arasteh PD, Hosseini A. Assessment of urban heat island based on the relationship between land surface temperature and land use/land cover in Tehran. Sustainable Cities and Society 2016;23:94-104.

Bonafoni S, Anniballe R, Gioli B, Toscano P. Downscaling Landsat land surface temperature over the urban area of Florence. European Journal of Remote Sensing 2016;49(1):553-69.

Brammer H. Physical Geography of Bangladesh. Dhaka, Bangladesh: The University Press Ltd.; 2012.

Brammer H. The Geography of the Soils of Bangladesh. Dhaka, Bangladesh: The University Press Ltd.; 1996.

Butler K. Band Combinations for Landsat 8 [Internet]. 2013 [cited 2020 Feb 17]. Available from: https://blogs.esri.com/esri/arcgis/2013/07/24/band-combinations-for-landsat-8/.

Chander G, Markham B. Revised Landsat-5 TM radiometric calibration procedures and postcalibration dynamic ranges. IEEE Transactions on Geoscience and Remote Sensing 2003;41(11):2674-7.

Chander G, Markham BL, Helder DL. Summary of current radiometric calibration coefficients for Landsat MSS, TM, ETM+, and EO-1 ALI sensors. Remote Sensing of Environment 2009;113(5):893-903.

Chen XL, Zhao HM, Li PX, Yin ZY. Remote sensing image-based analysis of the relationship between urban heat island and land use/cover changes. Remote Sensing of Environment 2006;104(2):133-46.

Corner RJ, Dewan AM, Chakma S. Monitoring and prediction of land-use and land-cover (LULC) change. In: Dewan AM, Corner RJ, editors. Dhaka Megacity. Dordrecht, Netherlands: Springer; 2014. p. 75-97.

Dereczynski CP, Luiz Silva W, Marengo JA. Detection and projections of climate change in Rio de Janeiro, Brazil. American Journal of Climate Change 2013;2:25-33.

Dewan AM, Corner RJ. Impact of land use and land cover changes on urban land surface temperature. In: Dewan AM, Corner RJ, editors. Dhaka Megacity. Dordrecht, Netherlands: Springer; 2014a. p. 219-38.

Dewan AM, Corner RJ. Spatiotemporal analysis of urban growth, sprawl and structure. In: Dewan AM, Corner RJ, editors. Dhaka Megacity. Dordrecht, Netherlands: Springer; 2014b. p. 99-121.

Erener A. Classification method, spectral diversity, band combination and accuracy assessment evaluation for urban feature detection. International Journal of Applied Earth Observation and Geoinformation 2013;21:397-408.

Gazi MY, Rahman MZ, Uddin MM, Rahman FA. Spatio-temporal dynamic land cover changes and their impacts on the urban thermal environment in the Chittagong metropolitan area, Bangladesh. GeoJournal 2020;24:1-6.

Grimmond SU. Urbanization and global environmental change: Local effects of urban warming. Geographical Journal 2007;173(1):83-8.

Guha S, Govil H, Diwan P. Analytical study of seasonal variability in land surface temperature with normalized difference vegetation index, normalized difference water index, normalized difference built- up index, and normalized multiband drought index. Journal of Applied Remote Sensing 2019;13(2):Article No. 024518.

Han-Qiu XU. A study on information extraction of water body with the modified normalized difference water index (MNDWI). Journal of Remote Sensing 2005;5:589-95.

Hasan SS, Deng X, Li Z, Chen D. Projections of future land use in Bangladesh under the background of baseline, ecological protection and economic development. Sustainability 2017;9(4):Article No. 505.

Huete A, Didan K, van Leeuwen W, Miura T, Glenn E. MODIS vegetation indices. In: Ramachandran B, Justice CO, Abrams MJ, editors. Land Remote Sensing and Global Environmental Change. New York, USA: Springer; 2010. p. 579-602.

Intergovernmental Panel on Climate Change (IPCC). Climate Change 2014: Mitigation of Climate Change. In: Contribution of Working Group III to the Fifth Assessment Report of the Intergovernmental Panel on Climate Change. New York, USA: Cambridge University Press; 2014.

Jiménez-Muñoz JC, Sobrino JA, Skoković D, Mattar C, Cristóbal J. Land surface temperature retrieval methods from Landsat-8 thermal infrared sensor data. IEEE Geoscience and Remote Sensing Letters 2014;11(10):1840-3.

Kabir A. Mymensingh Strategic Development 2011-2035 [Internet]. 2015 [cited 2020 Mar 10]. Available from: http://msdp.gov.bd/reports/category/13.

Kafy AA, Rahman MS, Hasan MM, Islam M. Modelling future land use land cover changes and their impacts on land surface temperatures in Rajshahi, Bangladesh. Remote Sensing Applications: Society and Environment 2020;18: Article No. 100314.

Kayet N, Pathak K, Chakrabarty A, Sahoo S. Urban heat island explored by co-relationship between land surface temperature vs multiple vegetation indices. Spatial Information Research 2016;24(5):515-29.

Kikon N, Singh P, Singh SK, Vyas A. Assessment of urban heat islands (UHI) of Noida City, India using multi-temporal satellite data. Sustainable Cities and Society 2016;22:19-28.

Lai LW, Cheng WL. Urban heat island and air pollution: An emerging role for hospital respiratory admissions in an urban area. Journal of Environmental Health 2010;72(6):32-6.

Li YY, Zhang H, Kainz W. Monitoring patterns of urban heat islands of the fast-growing Shanghai metropolis, China: Using time-series of Landsat TM/ETM+ data. International Journal of Applied Earth Observation and Geoinformation 2012; 19:127-38.

Li ZL, Tang BH, Wu H, Ren H, Yan G, Wan Z, et al. Satellite-derived land surface temperature: Current status and perspectives. Remote Sensing of Environment 2013;131:14-37.

Maduako ID, Yun Z, Patrick B. Simulation and prediction of land surface temperature (LST) dynamics within Ikom City in Nigeria using artificial neural network (ANN). Journal of Remote Sensing and GIS 2016;5(1):1-7.

Maimaitiyiming M, Ghulam A, Tiyip T, Pla F, Latorre-Carmona P, Halik Ü, et al. Effects of green space spatial pattern on land surface temperature: Implications for sustainable urban planning and climate change adaptation. ISPRS Journal of Photogrammetry and Remote Sensing 2014;89:59-66.

Markham BL, Barker JL. Spectral characterization of the Landsat Thematic Mapper sensors. International Journal of Remote Sensing 1985;6(5):697-716.

McCarthy MP, Best MJ, Betts RA. Climate change in cities due to global warming and urban effects. Geophysical Research Letters 2010;37(9):Article No. L09705.

Mishra VN, Rai PK, Prasad R, Punia M, Nistor MM. Prediction of spatio- temporal land use/land cover dynamics in rapidly developing Varanasi District of Uttar Pradesh, India, using geospatial approach: A comparison of hybrid models. Applied Geomatics 2018;10(3):257-76.

Mishra VN, Rai PK. A remote sensing aided multi-layer perceptron-Markov chain analysis for land use and land cover change prediction in Patna District (Bihar), India. Arabian Journal of Geosciences 2016;9(4):Article No. 249.

National Aeronautics and Space Administration (NASA). NASA's Atmospheric Correction Parameter Calculator [Internet]. 2019 [cited 2020 Feb 17]. Available from: http://atmcorr.gsfc.nasa.gov/.

Pal S, Ziaul SK. Detection of land use and land cover change and land surface temperature in English Bazar urban centre. Egyptian Journal of Remote Sensing and Space Science 2017;20(1):125-45.

Qin Z, Karnieli A, Berliner P. A mono-window algorithm for retrieving land surface temperature from Landsat TM data and its application to the Israel-Egypt border region. International Journal of Remote Sensing 2001;22(18):3719-46.

Rahman MT, Aldosary AS, Mortoja M. Modeling future land cover changes and their effects on the land surface temperatures in the Saudi Arabian eastern coastal city of Dammam. Land 2017;6(2):Article No. 36.

Rashid KJ, Hoque MA, Esha TA, Rahman MA, Paul A. Spatiotemporal changes of vegetation and land surface temperature in the refugee camps and its surrounding areas of Bangladesh after the Rohingya influx from Myanmar. Environment, Development and Sustainability 2021; 23(3):3562-77.

Rosa W. Goal 11: Make cities and human settlements inclusive, safe, resilient, and sustainable. In: Rosa W, editor. A New Era in Global Health: Nursing and the United Nations 2030 Agenda for Sustainable Development. New York, USA: Springer Publishing Company; 2017. p. 339-44.

Rouf MA, Jahan S. Spatial and Temporal Patterns of Urbanization in Bangladesh. Urbanization in Bangladesh: Patterns, Issues and Approaches to Planning. Dhaka, Bangladesh: Bangladesh Institute of Planners; 2007. p. 1-24.

Roy DP, Wulder MA, Loveland TR, Woodcock CE, Allen RG, Anderson MC, et al. Landsat-8: Science and product vision for terrestrial global change research. Remote Sensing of Environment 2014;145:154-72.

Roy PS, Miyatake S, Rikimaru A. Biophysical spectral response modeling approach for forest density stratification. Proceedings of the 18th Asian Conference on Remote Sensing; 1997 Oct 20-24; Kuala Lumpur: Malaysia; 1997.

Roy S, Farzana K, Papia M, Hasan M. Monitoring and prediction of land use/land cover change using the integration of Markov chain model and cellular automation in the Southeastern Tertiary Hilly Area of Bangladesh. International Journal of Sciences: Basic and Applied Research 2015;24:125-48.

Roy S, Mahmood R. Monitoring shoreline dynamics using Landsat and hydrological data: A case study of Sandwip Island of Bangladesh. Pennsylvania Geographer 2016;54(2):20-41.

Roy S, Pandit S, Eva EA, Bagmar MS, Papia M, Banik L, et al. Examining the nexus between land surface temperature and urban growth in Chattogram Metropolitan Area of Bangladesh using long term Landsat series data. Urban Climate 2020;32:Article No. 100593.

Salisbury JW, D'Aria DM. Emissivity of terrestrial materials in the 3-5 μm atmospheric window. Remote Sensing of Environment 1994;47(3):345-61.

Scarano M, Sobrino JA. On the relationship between the sky view factor and the land surface temperature derived by Landsat-8 images in Bari, Italy. International Journal of Remote Sensing 2015;36(19-20):4820-35.

Sobrino JA, Jiménez-Muñoz JC, Paolini L. Land surface temperature retrieval from LANDSAT TM 5. Remote Sensing of Environment 2004;90(4):434-40.

Sobrino JA, Raissouni N. Toward remote sensing methods for land cover dynamic monitoring: Application to Morocco. International Journal of Remote Sensing 2000;21(2):353-66.

Solecki WD, Rosenzweig C, Parshall L, Pope G, Clark M, Cox J, et al. Mitigation of the heat island effect in urban New Jersey. Global Environmental Change Part B: Environmental Hazards 2005;6(1):39-49.

Trenberth KE. Rural land-use change and climate. Nature 2004;427(6971):Article No. 213.

Ullah S, Tahir AA, Akbar TA, Hassan QK, Dewan A, Khan AJ, et al. Remote sensing-based quantification of the relationships between land use land cover changes and surface temperature over the Lower Himalayan Region. Sustainability 2019; 11(19):Article No. 5492.

United Nations (UN). World Population Prospects 2019: Highlights. Department of Economic and Social Affairs [Internet]. 2019 [cited 2020 Mar 10]. Available from: https://www.un.org/development/desa/publications/world-population-prospects-2019-highlights.html.

United Nations (UN). World Population Prospects: The 2017 Revision, Key Findings and Advance Tables. New York, USA: The United Nations; 2017.

United Nations Human Settlement Programme (UNHABITAT). Urbanization and Development: Emerging Futures. World cities report. Nairobi, Kenya: United Nations Human Sttlements Programme; 2016.

United States Geological Survey (USGS). Changes to Thermal Infrared Sensor (TIRS) data. Landsat 8 OLI and TIRS Calibration Notices [Internet]. 2014 [cited 2020 Feb 5]. Available from: https://www.usgs.gov/land-resources/nli/landsat/landsat-8-oli-and-tirs-calibration-notices.

United States Geological Survey (USGS). Landsat 7 (L7) Data Users Handbook. South Dakota, USA: Earth Resources Observation and Science (EROS); 2019.

Van de Griend AA, OWE M. On the relationship between thermal emissivity and the normalized difference vegetation index for natural surfaces. International Journal of Remote Sensing 1993;14(6):1119-31.

Vani M, Prasad PR. Assessment of spatio-temporal changes in land use and land cover, urban sprawl, and land surface temperature in and around Vijayawada city, India. Environment, Development and Sustainability 2020; 22(4):3079-95.

Veronez MR, Thum AB, Luz AS, Da Silva DR. Artificial neural networks applied in the determination of soil surface temperature-SST. Proceedings of the 7th International Symposium on Spatial Accuracy Assessment in Natural Resources and Environmental Sciences; 2006 Jul 5-7; Portugal, New University of Lisbon: 2006. p. 889-98.

Voogt JA, Oke TR. Thermal remote sensing of urban climates. Remote Sensing of Environment 2003;86(3):370-84.

Weng Q. A remote sensing? GIS evaluation of urban expansion and its impact on surface temperature in the Zhujiang Delta, China. International Journal of Remote Sensing 2001; 22(10):1999-2014.

World Bank. World Bank staff estimates based on the United Nations Population Division's World Urbanization Prospects [Internet]. 2018 [cited 2020 Mar 10]. https://data.worldbank.org/indicator/sp.urb.totl.in.zs.

Xu H, Ding F, Wen X. Urban expansion and heat island dynamics in the Quanzhou region, China. IEEE Journal of Selected Topics in Applied Earth Observations and Remote Sensing 2009;2(2):74-9.

Yu X, Guo X, Wu Z. Land surface temperature retrieval from Landsat 8 TIRS: Comparison between radiative transfer equation- based method, split window algorithm and single channel method. Remote Sensing 2014;6(10):9829-52.

Zanter K. Landsat 8 (L8) Data Users Handbook Survey [Internet]. 2015 [cited 2020 Mar 10]. Available from: https://www.usgs.gov/core-science-systems/nli/landsat/landsat-8-data-users-handbook.

Zareie S, Khosravi H, Nasiri A, Dastorani M. Using Landsat Thematic Mapper (TM) sensor to detect change in land surface temperature in relation to land use change in Yazd, Iran. Solid Earth 2016;7(6):1551-64.

Zha Y, Gao J, Ni S. Use of normalized difference built- up index in automatically mapping urban areas from TM imagery. International Journal of Remote Sensing 2003;24(3):583-94.

Zhang F, Tiyip T, Kung H, Johnson VC, Maimaitiyiming M, Zhou M, et al. Dynamics of land surface temperature (LST) in response to land use and land cover (LULC) changes in the Weigan and Kuqa River oasis, Xinjiang, China. Arabian Journal of Geosciences 2016;9(7):1-4.